Visualization of nanocrystalline CuO in the grain boundaries of Cu 2 O thin films and effect on band bending and film resistivity

Jonas Deuermeier, Hongjun Liu, Laetitia Rapenne, Tomás Calmeiro, Gilles Renou, Rodrigo Martins, David Munoz-Rojas, Elvira Fortunato

Visualization of nanocrystalline CuO in the grain boundaries of Cu_2O thin films and effect on band bending and film resistivity

Jonas Deuermeier,[1,a] Hongjun Liu,[2] Laetitia Rapenne,[2] Tomás Calmeiro,[1] Gilles Renou,[3] Rodrigo Martins,[1] David Muñoz-Rojas,[2,b] and Elvira Fortunato[1]

[1]*i3N/CENIMAT, Department of Materials Science, Faculty of Science and Technology, Universidade NOVA de Lisboa and CEMOP/UNINOVA, Campus de Caparica, 2829-516 Caparica, Portugal*
[2]*Université Grenoble Alpes, CNRS, Grenoble INP, LMGP, F-38000 Grenoble, France*
[3]*Université Grenoble Alpes, CNRS, SIMAP, F-38042 Saint-Martin d'Hères, France*

(Received 29 May 2018; accepted 9 August 2018; published online 7 September 2018)

Direct evidence for the presence of a CuO structure in the grain boundaries of Cu_2O thin films by chemical vapor deposition is provided by high resolution automated phase and orientation mapping (ASTAR), which was not detectable by classical transmission electron microscopy techniques. Conductive atomic force microscopy (CAFM) revealed that the CuO causes a local loss of current rectification at the Schottky barrier between the CAFM tip and Cu_2O. The suppression of CuO formation at the Cu_2O grain boundaries is identified as the key strategy for future device optimization. https://doi.org/10.1063/1.5042046

The p-type oxide semiconductor Cu_2O has a band gap of 2.09 eV and a wide range of carrier concentrations is reported in the literature (10^9–10^{16} cm^{-3}).[1–5] These characteristics allow different kinds of applications such as photovoltaics, photocatalysis, thin-film transistors, or resistive switching devices.[6–8] However, the material is only metastable at room temperature and ambient pressure and shows a tendency to form precipitates of secondary phases.[9–11] The formation of secondary phases is typically controlled by process parameters, which influence the thermodynamics and kinetics of the deposition.[12,13] In addition, it is still debated whether the observation of Cu(II) on the surface of air-exposed Cu_2O films by XPS[11,14–16] corresponds to the presence of a CuO native layer. For maximum conversion efficiencies of photovoltaic devices, the formation of CuO at the interface between Cu_2O and the n-type layer needs to be avoided.[14]

The presence of secondary phases has a tremendous effect on the transport properties of the material. The grain boundaries in polycrystalline Cu_2O are known to be more conductive than the grain interior.[17] In thin films, oxidation of the copper ions to Cu(II) at low film thicknesses was observed by X-ray photoelectron spectroscopy.[18] Since CuO has a band gap of 1.5 eV and a carrier concentration of 10^{19} cm^{-3},[19,20] the increased conductivity in the grain boundaries was ascribed to the presence of Cu(II).[18] However, no evidence for the existence of a CuO structure was provided.

In the present study, high resolution transmission electron microscopy (TEM) based automatic phase mapping was used to identify the crystal structure at the grain boundaries of Cu_2O thin films deposited by aerosol assisted metal organic chemical vapor deposition (AA-MOCVD) with a point-to-point resolution of 0.25 nm. Conductive atomic force microscopy (CAFM) was used to investigate the local current transport characteristics of the polycrystalline Cu_2O films.

[a]Electronic mail: j.deuermeier@campus.fct.unl.pt
[b]Electronic mail: david.munoz-rojas@grenoble-inp.fr

The Cu_2O thin films were deposited in a homemade aerosol assisted metal organic chemical vapor deposition (AA-MOCVD) system. Copper(II) trifluoroacetylacetonate (98%, Strem Chemical) was used as the precursor and ethanol as the solvent. A 0.01 M solution was prepared by mixing 1.85 g of the precursor in 0.5 l of solvent, following with 10 min magnetic bar stirring. The depositions were conducted for 220 min at 335 °C with additional samples prepared at 305 °C and 350 °C. During the deposition, the consumption rate of the precursor solution was maintained at around 1.5 ml/min. Gas flows were 2 l/min N_2 (carrier gas 1) and 5 l/min air with 3 l/min N_2 (carrier gas 2). The pressure in the deposition chamber was close to atmospheric pressure. Different substrates were used: samples for TEM/ASTAR characterization were deposited on silicon whereas CAFM measurements were conducted on films deposited on indium-tin oxide (ITO) coated glass. Corning glass was used for X-ray diffraction and Raman measurements reported in the supplementary material.

The morphology and structural properties of Cu_2O thin films were investigated by transmission electron microscopy with a JEOL 2010 LaB6 microscope operating at 200 kV with a 0.19 nm point-to-point resolution. In addition, a JEOL 2100F FEG TEM equipped with the precession assisted automated crystal phase and orientation mapping tool ASTAR from NanoMEGAS was used.[21,22]

An Asylum Research MFP-3D atomic force microscope was used to obtain topographies, local current-voltage characteristics, and current maps. The latter were measured in contact mode with the voltage applied to the chuck while the tip (Nanoworld CONTPt) remained at ground potential. In order to evaluate the electrical properties of the Cu_2O/ITO interface with an Agilent 4155C semiconductor parameter analyzer, Ohmic top contacts of 5 nm Ni and 60 nm Au were deposited through shadow masks by electron beam evaporation.

TEM results of a deposited Cu_2O film are presented in Figs. 1(a) and 1(b). A cross section image of the Cu_2O thin film is shown in Fig. 1(a), in which columnar-like grains are oriented perpendicular to the substrate. The length of the grains can reach almost 1 μm. Figure 1(b) presents the selected area electron diffraction (SAED) pattern in the vicinity of the grain boundaries. From the diffraction

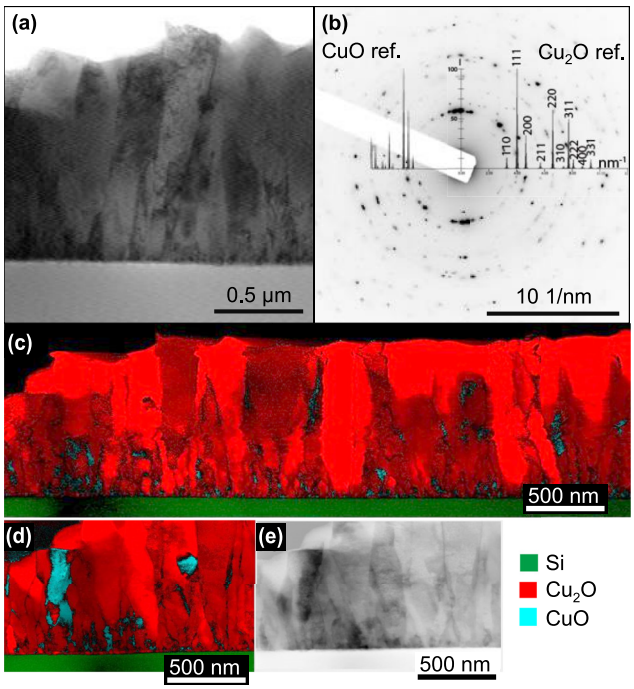

FIG. 1. TEM characterization of Cu_2O films deposited at 335 °C. (a) STEM annular dark field cross section image, showing columnar growth. (b) SAED pattern of a region near the Cu_2O grain boundary with the CuO C2/c (15) reference pattern on the left and the Cu_2O cubic Pn-3m (224) reference pattern on the right. [(c) and (d)] Automatic crystal orientation/phase (ASTAR) mapping of the Cu_2O thin film cross section. The red color corresponds to the Cu_2O structure, the blue color represents the CuO structure, and the green color refers to the silicon substrate. (e) Reconstructed correlation gray scale index map related to (d).

pattern, the Cu_2O structure was observed, showing a preferential orientation with (111) planes parallel to the substrate surface. By comparing the obtained diffraction pattern with the CuO reference [as shown in Fig. 1(b)], no diffraction reflections associated with the CuO structure could be found in the deposited Cu_2O film by SAED. Other commonly used techniques such as X-ray diffraction and Raman spectroscopy were also used and no CuO was detected (see the supplementary material).

The cross section of the deposited Cu_2O film was characterized by the ASTAR technique. The precession angle used in the experiments was 1.16°. The diffraction patterns were obtained with a step size of 1 nm. The obtained phase maps are presented in Figs. 1(c)–1(e). Three phases were identified—marked with red, blue, and green—corresponding to Cu_2O, CuO, and silicon, respectively. Note that no CuO can be detected on the surface of the films. From the cross section, columnar Cu_2O grains with a width of about 400 nm and a length of 1 μm are observed, similar to the TEM results shown in Fig. 1(a). The closer view of the phase mapping in Fig. 1(d) clearly shows that the blue colored CuO phase is mostly located at the grain boundaries. In particular, the amount of CuO is significantly larger near the interface between the substrate and the Cu_2O film, where the Cu_2O grain size is smaller. The existence of the CuO phase in the grain boundaries is in line with the results obtained with XPS, which showed the presence of Cu(II).[18] The reconstructed correlation index map is presented in Fig. 1(e). The gray scale map was obtained by plotting the value of the correlation index for the succession of the electron diffraction patterns at each location. It indicates that the obtained phase mapping data have rather good reliability.

The CAFM results are shown in Fig. 2; (a) and (b) show a sample deposited at 305 °C measured with a positive bias applied to the substrate (2 V), whereas (c) and (d) show a sample deposited at 335 °C measured under negative bias (−2 V). The mask overlays in the topographies of Figs. 2(a) and 2(c) represent the areas of relatively high current. The corresponding current maps are presented in Figs. 2(b) and 2(d). In Fig. 2(d), only current values smaller than −400 pA are shown for better contrast although the maximum current reached to −10 nA. The current-voltage characteristics in Fig. 2(e) were measured after immobilizing the AFM tip at the locations marked in Figs. 2(c) and 2(d) with the red (grain) and blue (grain boundary) crosses. The average of 10 consecutive

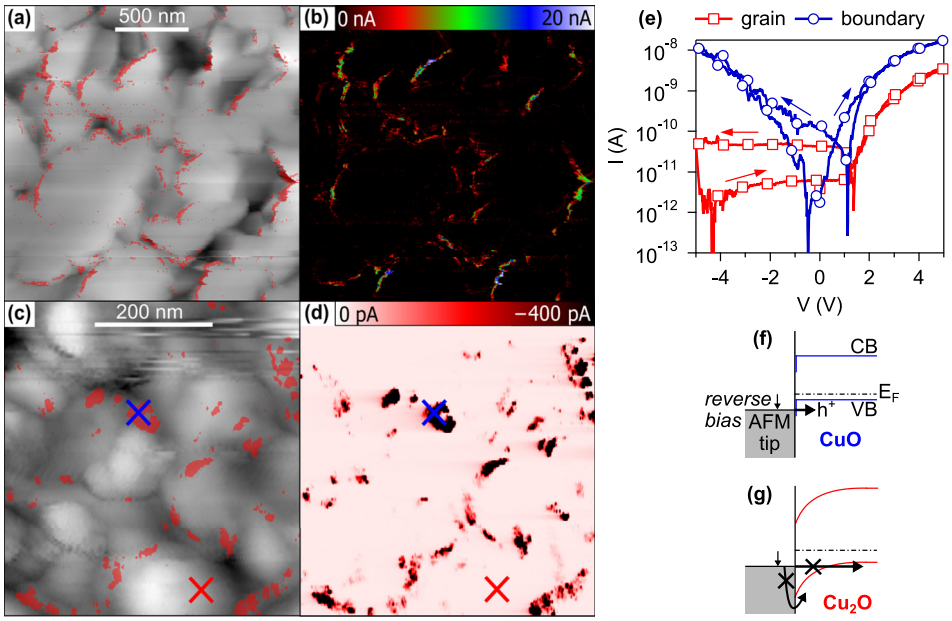

FIG. 2. (a) Topography and (b) current map biased at 2 V of a sample deposited at 305 °C. (c) Topography and (d) current map biased at −2 V of a sample deposited at 335 °C. In the topographies, the mask overlays in light red show areas of high current. The red (grain) and blue (grain boundary) crosses indicate the positions where the current-voltage characteristics were measured, which are shown in (e). Schematic representations of the energy band alignment (f) with the grain boundary region and (g) the grain region under reverse bias.

double sweeps between 0 V and +5 V, followed by 0 V and −5 V, was calculated. A general accordance between grain boundary regions in the topographies and the areas of high conductance is observed. Note that an increased current level in the grain boundary regions could be an artifact related to the increased contact area in the grain boundary region due to the surface topography. However, the barrier under negative substrate bias is only observed in the grain region. A CAFM study reported in the literature revealed a Schottky barrier between the cantilever tip and the surface of doped silicon, which disappeared when the sample was illuminated by the laser of the AFM with a photon energy above the band gap of silicon (1.85 eV).[23] In the case of our samples, conducting the current-voltage measurement of the grain boundary region in the dark (without the AFM laser emitting with an energy of 1.44 eV nor ambient light) showed no influence on the current rectification. Hence, photo-induced carriers are excluded as a reason for the absence of a barrier between the AFM tip and the grain boundaries. In order to investigate the influence of the interface between ITO and Cu_2O, the macroscopic current-voltage characteristics of the structure ITO/Cu_2O/Ni/Au were studied, revealing no current rectification (not shown).

As observed in Fig. 1, the density of grain boundaries is significantly increased towards the substrate interface. Due to the pinned Fermi level in CuO and the degeneracy of ITO, the ITO/CuO junction does not show current rectification.[19] This means that the current which is probed at the surface of a Cu_2O grain is shunted by the CuO in the grain boundaries in the vicinity to the substrate interface. This is in accordance with the high conductivity observed in copper oxide films at low thicknesses.[18] As a consequence, the rectification observed in Fig. 2(e) is related to the current transport over the interface between the copper oxide surface and the AFM tip. This is in line with the absence of a CuO structure on the surface of the samples; see Fig. 1(a). Since the Cu(II) oxidation state is detected by XPS of air-exposed Cu_2O samples,[11,14,16] the copper oxidation must be mainly caused by the adsorbates from the ambient air.

The work function of the platinum-iridium coating of the AFM tip is 5.3–5.5 eV, Cu_2O has a work function of around 5.0 eV, and CuO of has a work function of 4.7–5.5 eV.[19,24,25] Hence, based on the Schottky-Mott rule, none of the copper oxides should form a barrier with the AFM tip material. Most probably, surface states of Cu_2O cause the observed barrier, but the exact origin cannot be clarified here.

The Fermi level in the CuO grain boundary is pinned, which allows no band bending at the unbiased contact between AFM tip and CuO. The upper limit for the hole barrier height is given by the Fermi level with respect to the valence band maximum in CuO of 0.1 eV.[18,19] Contrarily, Cu_2O is able to show considerable band bending and can form Schottky barrier heights of 0.5 eV with a wide depletion region with respect to the film thickness.[11,26]

Figures 2(f) and 2(g) schematically illustrate the local energy band alignment between the AFM tip and the different copper oxides under reverse bias (negative voltage). A rough estimation of the dominant current transport mechanism can be made by means of comparing the tunneling parameter E_{00} [see Eq. (1)] with the thermal energy kT, where k is the Boltzmann constant and T is the temperature,[24,27]

$$E_{00} = \frac{q\hbar}{2}\sqrt{\frac{N}{m^*\epsilon}}. \tag{1}$$

Here, q is the charge, $\hbar$ is the reduced Planck constant, N is the intrinsic acceptor concentration, m^* is the effective mass, and ϵ is the dielectric constant.

The condition for tunneling $E_{00} \gg kT$ implies a minimum acceptor concentration at a given temperature, here room temperature. For the case of tunneling in CuO with $m^* = 7.9\ m_0$ and $\epsilon = 10.5\ \epsilon_0$,[20,28] $N \gg 2 \times 10^{20}$ cm^{-3}. m_0 is the free electron mass at rest and ϵ_0 is the vacuum permittivity. Acceptor concentrations in CuO are not available in the literature. The reported hole carrier concentrations at room temperature range between 10^{19} cm^{-3} and 6×10^{20} cm^{-3}.[19,20] Based on these values, it can be assumed that the condition for tunneling is fulfilled since the acceptor concentration is always equal or higher than the hole concentration. Hence, tunneling can explain the exponential voltage dependence in reverse bias, which is observed in Fig. 2(e). Due to the high intrinsic acceptor concentration of the material, the barrier at the interface to the AFM tip is very thin, which is schematically illustrated in Fig. 2(f).

For Cu_2O, the condition for tunneling is $N \gg 7 \times 10^{18}$ cm^{-3} using $m^* = 0.58\, m_0$ and $\epsilon = 7\, \epsilon_0$.[29,30] Reported acceptor concentrations range from 10^{14} cm^{-3} to 10^{18} cm^{-3}.[4,26,31,32] Hence, thermionic emission is the dominant mechanism for current transport in the reverse direction. Due to the high barrier in comparison to the thermal energy at room temperature and the wide depletion region in Cu_2O, the current in the reverse direction remains below the detection limits of the instrument; see Fig. 2(e). The efficient current blocking is schematically illustrated in Fig. 2(g).

In conclusion, the existence of nanometric CuO between the grains of Cu_2O was visualized by TEM high resolution automated phase and orientation mapping. The electric properties of the thin films were deconvoluted into the contributions of grains and grain boundaries by conductive AFM. A high grain boundary density causes junction characteristics to be dominated by shunting paths of nanocrystalline CuO and only its absence allows us to observe the rectification expected from Cu_2O. The presented results obtained from Cu_2O films deposited by AA-MOCVD corroborate previously published data on Cu_2O prepared by reactive radio-frequency magnetron sputtering.[18] As a consequence, it can be assumed that the existence of highly conductive CuO-containing grain boundaries in Cu_2O is a general characteristic of the material, independent of the deposition technique. Hence, to unlock the potential performance of this p-type oxide semiconductor, strategies to control/inhibit the formation of CuO in its grain boundaries must be considered.

See supplementary material for X-ray diffraction and Raman data of the Cu_2O films.

J.D. acknowledges FEDER funds through the COMPETE 2020 program and national funds through FCT–Portuguese Foundation for Science and Technology under the Project No. POCI-01-0145-FEDER-007688, reference UID/CTM/50025 as well as funding received from the European Union's Horizon 2020 research and innovation programme through the project HERACLES (Project No. 700395). H.L. acknowledges Manuel João Mendes for hosting him at CENIMAT and KIC Innoenergy and Ministère de l'Education nationale, de l'Enseignement supérieur et de la Recherche in France for the funding of this work. D.M.R. acknowledges funding through the Marie Curie Actions (FP7/2007-2013, Grant Agreement No. 631111). Transmission electron microscopy was performed at the CMTC characterization platform of Grenoble INP supported by the Centre of Excellence of Multifunctional Architectured Materials "CEMAM," No. ANR-10-LABX-44-01 funded by the "Investments for the Future" Program.

[1] R. Elliott, Phys. Rev. **108**, 1384 (1957).
[2] C. Malerba, F. Biccari, C. L. A. Ricardo, M. D'Incau, P. Scardi, and A. Mittiga, Sol. Energy Mater. Sol. Cells **95**, 2848 (2011).
[3] E. Fortin and F. L. Weichman, Can. J. Phys. **44**, 1551 (1966).
[4] Y. S. Lee, M. T. Winkler, S. C. Siah, R. Brandt, and T. Buonassisi, Appl. Phys. Lett. **98**, 192115 (2011).
[5] D. Muñoz-Rojas, M. Jordan, C. Yeoh, A. Marin, A. Kursumovic, L. Dunlop, D. Iza, A. Chen, H. Wang, and J. MacManus Driscoll, AIP Adv. **2**, 042179 (2012).
[6] B. K. Meyer, A. Polity, D. Reppin, M. Becker, P. Hering, P. J. Klar, T. Sander, C. Reindl, J. Benz, M. Eickhoff, C. Heiliger, M. Heinemann, J. Bläsing, A. Krost, S. Shokovets, C. Müller, and C. Ronning, Phys. Status Solidi B **249**, 1487 (2012).
[7] Z. Wang, P. K. Nayak, J. A. Caraveo-Frescas, and H. N. Alshareef, Adv. Mater. **28**, 3831 (2016).
[8] P. Yan, Y. Li, Y. Hui, S. Zhong, Y. Zhou, L. Xu, N. Liu, H. Qian, H. Sun, and X. Miao, Appl. Phys. Lett. **107**, 083501 (2015).
[9] M. Martinez-Clemente and R. D. Schmidt-Whitley, J. Mater. Sci. **10**, 543 (1975).
[10] F. L. Weichman, Can. J. Phys. **60**, 269 (1982).
[11] S. Siol, J. C. Hellmann, S. D. Tilley, M. Grätzel, J. Morasch, J. Deuermeier, W. Jaegermann, and A. Klein, ACS Appl. Mater. Interfaces **8**, 21824 (2016).
[12] A. Subramaniyan, J. D. Perkins, R. P. O'Hayre, S. Lany, V. Stevanovic, D. S. Ginley, and A. Zakutayev, APL Mater. **2**, 022105 (2014).
[13] F. M. Li, R. Waddingham, W. I. Milne, A. J. Flewitt, S. Speakman, J. Dutson, S. Wakeham, and M. Thwaites, Thin Solid Films **520**, 1278 (2011).
[14] R. L. Hoye, R. E. Brandt, Y. Ievskaya, S. Heffernan, K. P. Musselman, T. Buonassisi, and J. L. MacManus-Driscoll, APL Mater. **3**, 020901 (2015).
[15] A. Chen, H. Long, X. Li, Y. Li, G. Yang, and P. Lu, Vacuum **83**, 927 (2009).
[16] A. Rosencwaig and G. Wertheim, J. Electron Spectrosc. Relat. Phenom. **1**, 493 (1972).
[17] F. L. Weichman, J. Appl. Phys. **41**, 3491 (1970).
[18] J. Deuermeier, H. F. Wardenga, J. Morasch, S. Siol, S. Nandy, T. Calmeiro, R. Martins, A. Klein, and E. Fortunato, J. Appl. Phys. **119**, 235303 (2016).
[19] J. Morasch, H. F. Wardenga, W. Jaegermann, and A. Klein, Phys. Status Solidi A **213**, 1615 (2016).
[20] A. A. Samokhvalov, N. A. Viglin, B. A. Gizhevskii, N. N. Loshkareva, V. V. Osipov, N. I. Solin, and Yu. P. Sukhorukov, J. Exp. Theor. Phys. **76**, 463 (1993).

[21] E. Rauch and M. Véron, Mater. Charact. **98**, 1 (2014).
[22] P. A. Midgley and A. S. Eggeman, IUCrJ **2**, 126 (2015).
[23] M. Rumler, M. Rommel, J. Erlekampf, M. Azizi, T. Geiger, A. J. Bauer, E. Meißner, and L. Frey, J. Appl. Phys. **112**, 034909 (2012).
[24] S. M. Sze, *Physics of Semiconductor Devices*, 3rd ed. (John Wiley & Sons, 2007).
[25] J. Deuermeier, J. Gassmann, J. Brötz, and A. Klein, J. Appl. Phys. **109**, 113704 (2011).
[26] W. H. Brattain, Rev. Mod. Phys. **23**, 203 (1951).
[27] A. Büyükbaş-Uluşan, A. Tataroğlu, Y. Azizian-Kalandaragh, and Ş. Altındal, J. Mater. Sci.: Mater. Electron. **29**, 159 (2018).
[28] T. Ito, H. Yamaguchi, K. Okabe, and T. Masumi, J. Mater. Sci. **33**, 3555 (1998).
[29] J. W. Hodby, T. E. Jenkins, C. Schwab, H. Tamura, and D. Trivich, J. Phys. C: Solid State Phys. **9**, 1429 (1976).
[30] P. Dawson, M. Hargreave, and G. Wilkinson, J. Phys. Chem. Solids **34**, 2201 (1973).
[31] M. Zouaghi, M. Tapiero, J. Zielinger, and R. Burgraf, Solid State Commun. **8**, 1823 (1970).
[32] A. Mittiga, F. Biccari, and C. Malerba, Thin Solid Films **517**, 2469 (2009).